Captive Continuous Inkjet

Carolyn Ellinger, Yonglin Xie; Eastman Kodak Company, 1999 Lake Avenue, Rochester, NY, USA

Abstract

Captive continuous inkjet (CIJ) is a potentially disruptive inkjet technology recently developed in the Kodak Technology Center. The captive continuous inkjet technology is expected to deliver the best of both drop-on-demand (DOD) inkjet and continuous inkjet (CIJ) technologies: high resolution, compact size, and low cost associated with traditional DOD technologies and the high throughput and high reliability of traditional CIJ technology. In this paper, we will provide a description of this new architecture, its function and why we believe it to be advantaged over both traditional CIJ and DOD technologies. We will discuss the key technology elements with details on the design, fabrication, and characterization of captive CIJ devices, including results from simulations and experimental studies.

Introduction

Captive continuous inkjet (CIJ) technology uses the momentum of an internal captive continuous ink flow in combination with a deflection mechanism to generate print drops by deflecting the internal flow out of a relatively large opening.[1,2,3,4,5] In operation, the continuous internal flow gives rise to drops with a momentum similar to other continuous inkjet technologies, and removes the firing frequency limitations that are associated with the capillary refill mechanism of typical DOD technologies. Also, unlike other continuous inkjet technologies, the fluid deflection mechanism is only employed when a print drop is required so there is no need for drop sorting after drop formation. These characteristics should translate into advantages in image quality, print speed, system cost, and ejector reliability.

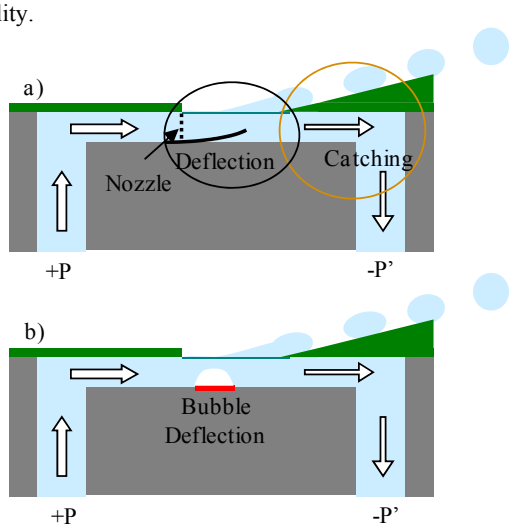

Figure 1. *Two variations of the captive CIJ architecture are shown. In a) a mechanical actuator is used to deflect the captive ink flow, while in b) the ink is deflected using a thermal vapor bubble.*

Figure 1 illustrates the captive CIJ architecture with two potential deflection mechanisms: a mechanical actuator as shown in a) and thermal bubble deflection as shown in b). A positive pressure is used to supply ink to a channel on the top surface of a silicon-based MEMS device. Figure 1 a) is labeled to indicate the components of the captive CIJ architecture which are analogous to traditional CIJ architectures. The traditional nozzle is not necessary in this new architecture, but is instead replaced by a fluidic channel as indicated in Figure 1 a), that is on the order of 13 x 20 μm^2 in cross section. The traditional drop sorting / deflection mechanism used in CIJ technologies is replaced here with an actuator which causes the fluid in the channel to be deflected out of a large bore in the top of the device channel when print drops are requested, but allows the fluid to flow unimpeded during times of non-print. Traditional CIJ technologies have external catcher mechanisms to catch non-print drops after deflection. In contrast, the non-print condition for continuous CIJ is flow in the exit (or catching) channel removing the need for the external element.

Image quality gains are predicted from the ability of the captive CIJ technology to form small drop volumes at high drop velocities. Drop volumes ranging from sub-1 pL to 10 pL are possible, and variable levels of actuation generate variable drop volumes. These drops have high velocity (10 – 30 m/s), resulting in high drop momentum and short flight times. Without the need for external deflection hardware, the drop generator can be placed close to the substrate further helping to ensure accurate drop placement. Additionally, the architecture is amenable to high nozzle density which will allow high resolution implementation. The captive CIJ architecture can form print drops at high frequencies, ranging from 1 kHz to 500 kHz lending itself to use at high print (paper) speeds even at high resolution. When compared with other continuous inkjet technologies the integrated-on-chip deflector and catcher translate into much simpler system with much lower projected costs. Additionally, the continuous flow of ink will prevent ink from drying out in drop ejector, which should foster reliable drop formation.

With guidance provided from initial modeling, we set out to reduce the captive CIJ architecture to practice and built real working inkjet devices. There are two key concepts that are critical for the captive CIJ architecture to function properly: 1) the ink must remain captive when print drops are not desired and 2) the deflection mechanism and device architecture must cleanly eject a drop when a print drop is desired. Both requirements were experimentally unproved at the onset of this project, and therefore it was useful to initially decouple the captive flow from the fluid ejection mechanism. Two MEMS designs, as illustrated in Figure 2 a) and b), were fabricated and evaluated to determine if each requirement could be met independently prior to building an integrated device.

©2013; Society for Imaging Science and Technology

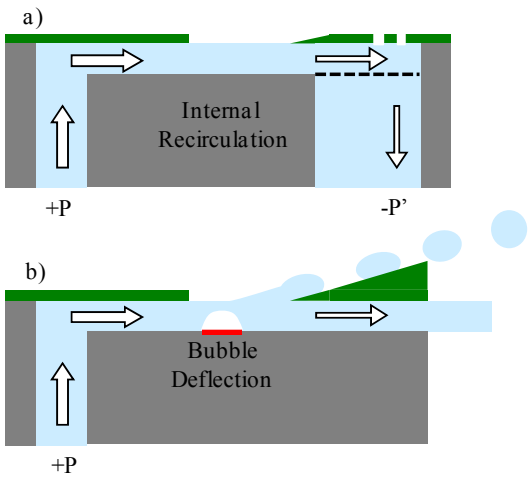

Figure 2. *Schematics for initial device evaluation are shown; a) captive flow architecture containing no deflection mechanism and b) drop formation architecture using a thermal vapor bubble actuator to deflect the ink, but having no internal recirculation.*

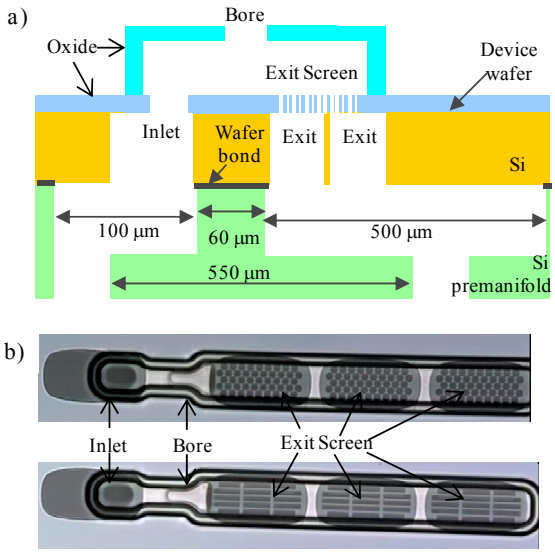

Figure 3. *Schematic of Captive flow architecture is shown in a). Optical micrograph images of completed captive flow devices are shown in b).*

Captive Flow: Device Design, Fabrication and Evaluation

To investigate captive flow in a single channel an experiment was designed. Geometric variations were included to provide an initial understanding of: 1) accelerating and controlling the fluid velocities under the top opening; 2) the channel length to establish stable flow; 3) necessary fluid deceleration at exit section; 4) sensitivity of the flow to inlet and outlet pressures; and 5) issues with air entrainment in the channel or exit section. Geometric channel parameters were varied in the experiment, and multiple device configurations were fabricated using standard MEMS processes to form captive channels with dielectric walls on 675 µm thick wafers, which were thinned to 350 µm prior to etching the ink feed channels by the anisotropic deep reactive ion etch (DRIE) process.[1] Additionally, stainless steel fluidic manifolds were designed and built to accommodate the requirement of controlled positive pressure for the ink feed and vacuum levels on the ink return. A schematic cross-section of the devices can be found in Figure 3 a). In order to facilitate packaging to the stainless steel manifold, a silicon premanifold was wafer bonded to the device wafer as shown in Figure 3 a). Figure 3 b) shows top view micrographs of two completed device variations. As illustrated, a number of exit screen variations were evaluated for their impact on captive recirculation.

These devices were tested using a clear test fluid (water, biocide and surfactant), as well as dye and pigment based inks. A positive pressure source was used to supply ink to the inlet of the device, over the range of 10 to 80 psi. The exit pressure was controlled using a vacuum regulator, and varied from atmospheric pressure (760 mmHg) to 300 mmHg.

Figure 4 a) shows the results of computation fluid dynamic modeling illustrating the flow in a cross-section of the channel. It was found that in order to maintain captive flow it was critical to create a flow profile which dipped under the end of the bore (ramp). This profile could be generated in most devices given a sufficient inlet fluid velocity (pressure) and in combination with exit flow expansion and deceleration (controlled by vacuum level and geometric parameters). Figure 4 b) contains three top view micrographs showing the flow profile generated as function of inlet pressure with constant exit pressure. The elongated triangular profile corresponds with the predicted flow profile (air/fluid interface) under the top surface of the channel shown in Figure 4 a).

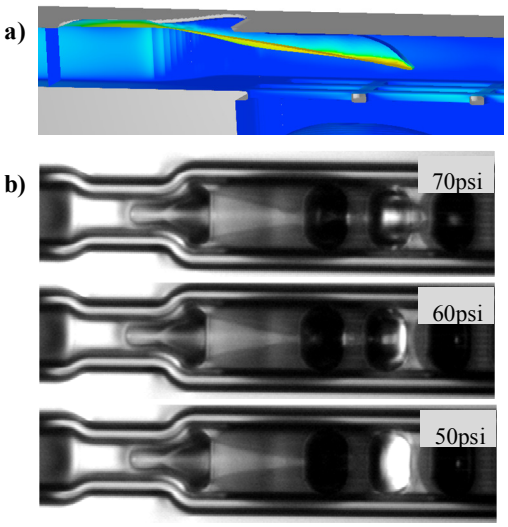

Figure 4. *Results from Computation fluid dynamics modeling using Flow3D are shown in a). Optical micrographs of the flow profile as a function of pressure for actual captive flow devices are shown in b).*

Drop Formation using a Solid Surface: Device Design, Fabrication and Evaluation

Proof-of-concept devices were fabricated to evaluate the novel drop formation mechanism. These devices employ thermal vapor bubble technology to deflect the flow of fluid in a channel without internal recirculation. The devices were designed as shown schematically in Figure 2 b) such that the non-deflected fluid exits the end of the channel and must be collected using an external fluid return path. This experiment provided the devices necessary to investigate the ability to form and control drops using a heater within a restrictive flow channel. Designs to probe 1) the interaction between fluid velocity and heater design; 2) the importance of the geometry of the bore and ramp set-back (RSB) for drop formation and control; 3) ramp shape used to launch the drop; and 4) the novel drop trajectory created by the captive CIJ drop formation mechanism were included. An overall understanding of the drop generation space including firing frequency, drop velocity and volume and drop stability was also obtained from these devices.

These devices were fabricated using standard MEMS processes on 675 µm thick wafers, which were thinned to 350 µm prior to etching the ink feed channels by the anisotropic deep reactive ion etch (DRIE) process.[1] The heaters were formed from TaN and the 13 µm tall channels were formed from a dielectric film (7 µm thick). Figure 5 a) shows and SEM image of a single channel, as shown each channel contains a split heater and a large bore opening in the top of the channel. Figure 5 b) shows the x-sectional schematic of the device oriented as tested – with the silicon surface mounted perpendicular to the ground.

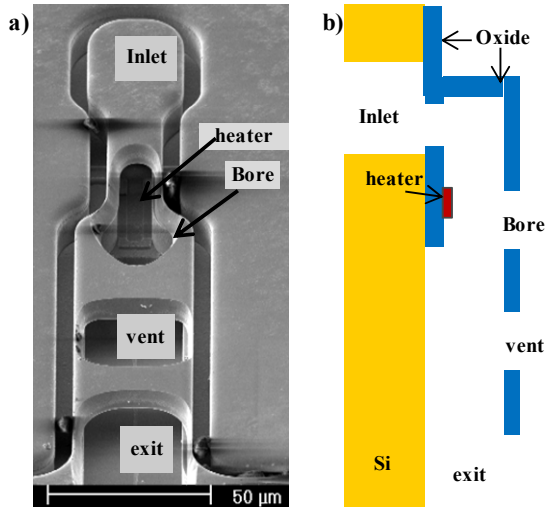

Figure 5. *SEM image of a single drop generating channel is shown in a). The corresponding schematic for the drop generator channel is shown in b).*

One of the goals of the experiment was to evaluate the shape and features of the bore on drop formation. The shape of the end of the bore, or ramp, was varied as shown in Figure 6. Three primary shapes were evaluated: angled as shown in a), flat as shown in b), and rounded as shown in c). Figure 6 also illustrates other design variables evaluated, including heater length, channel width, and ramp set back (RSB). The ramp set back is the distance from the end the heater to the end of the bore. The inlet and exit sections were kept constant, and the heater width was scaled with the channel width.

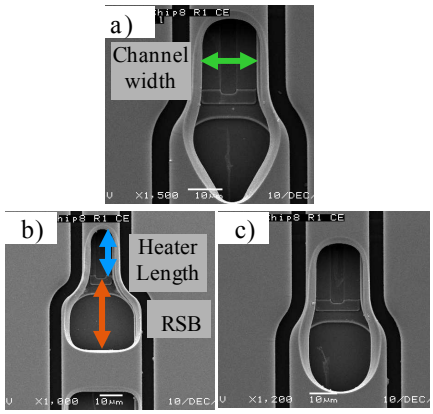

Figure 6 *SEM images of representative bore shapes: a) angled b) flat, and c) rounded.*

The novel drop formation of these devices required the development of a test fixture that was capable of imaging the drops. Ultimately, these devices were evaluated using both side view and front view optics in combination with standard stroboscopic methods, with the silicon mounted in a vertical orientation. The side view images provide the ability to assess the drop formation including drop volume, velocity and trajectory. Figure 7 illustrates a typical strobe delay series from these devices, with drop formation at 10kHz. As shown, the fluid in flowing through the channel from right to left, and each image is a time average view after the initiation of a voltage pulse to the heater. The stack of images shows the typical shallow trajectory found with these devices. Drop volume, velocity and trajectory were calculated after image processing for these and many other experimental images.

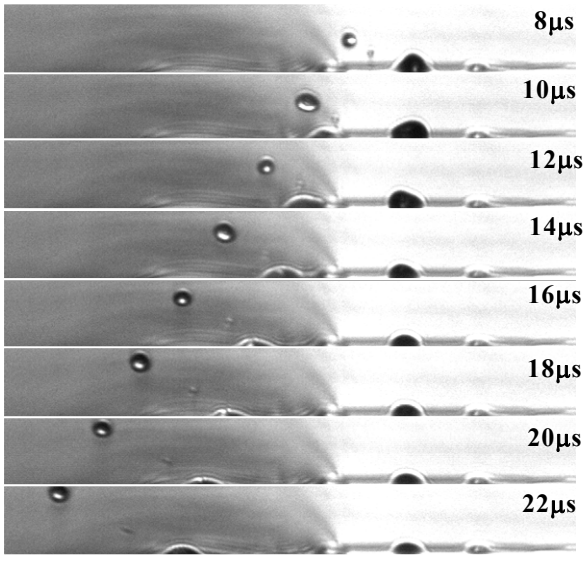

Figure 7. *Drop formation at 70psi at a series of delay times.*

©2013; Society for Imaging Science and Technology

Figure 8 contains data on the drop trajectory as measured from the channel top surface as a function of pressure. Some trends can be extracted from the data: 1) trajectory angle increases with increased pressure (increased flow), 2) larger channels could form drops at lower pressures (lower pressure required for equivalent channel velocity), and 3) drop formation was possible with angled and round bore designs (and not with the flat design shown in Figure 6 b)). Although it is less evident from the data in Figure 8, these devices have a threshold pressure for drop formation. Below the threshold pressure, the fluid momentum is insufficient to release a drop, regardless of the energy supplied to the heater.

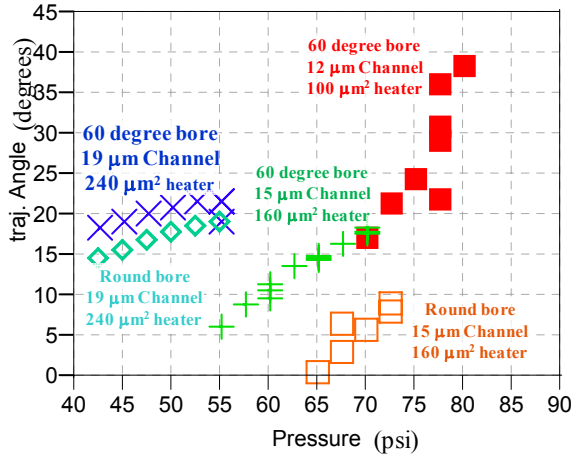

Figure 8. *Calculated drop trajectory as a function of inlet pressure for five different devices on a single die.*

Analysis of the same drops for velocity and volume is shown in Figure 9, illustrating the strong correlation between the various drop parameters. Generally, we found that the larger channels formed more stable drops. The larger channels also formed larger drops, and this drop volume increased with increased flow in the channel. These trends indicate that the amount of fluid that deflected controls the drop volume.

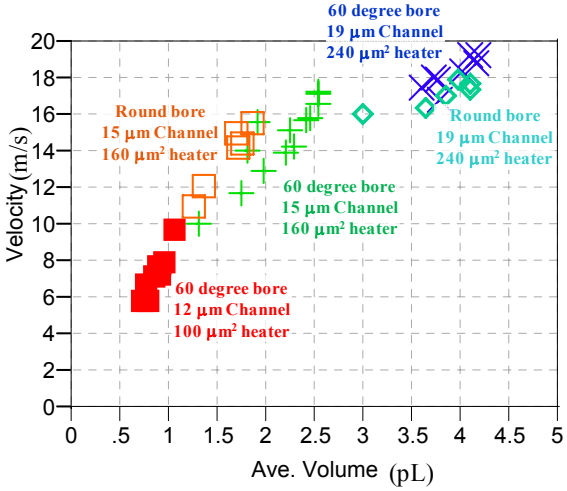

Figure 9. *Calcuated drop velocity as a function of drop volume for the pressure range shown in Figure 8. Drop velocity, volume and trajectory are highly correlated and dependant on geometry and fluid flow.*

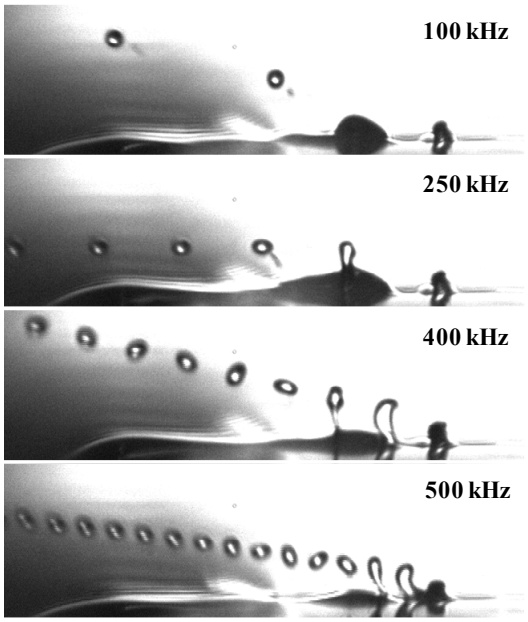

Figure 10. *Drop formation up to 500 kHz is shown, using a single channel device at 70psi with a 500 ns pulse a 10% over threshold energy.*

The majority of the testing was completed at a drop generation frequency of 10 kHz. In order to push the determine the limits on firing frequency, a single device was operated under 70psi, pulsing the heater with a fixed 500 ns pulse at 10% over the threshold energy required for drop formation. The frequency was increased until the device failed. Figure 10 shows stable drop formation from 100 kHz to 500 kHz. For the captive CIJ architecture, the drop formation frequency is the print drop formation frequency; implying that captive CIJ in a single array embodiment would be able to print at very high web speeds – over 2000 fpm at 1200 dpi. This result was surprising, and we turned to using the front view optics to visualize the bubble dynamics to better understand the fundamental drop formation limitations for this new architecture

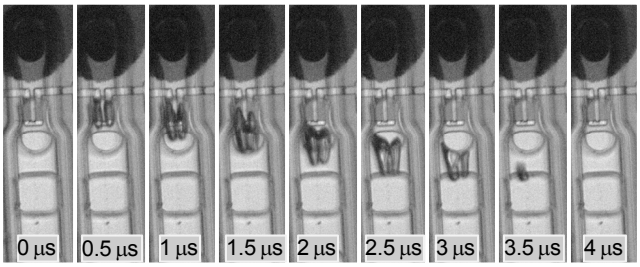

Figure 11. *The lifecycle of a bubble is shown at a series of delay times.*

Figure 11 shows the life cycle of the thermal vapor bubble used to deflect the captive fluid in the captive CIJ architecture. Each image is taken at a given delay (as indicated on the image) from the onset of the heater pulse. The heater pulse for these images was 500 ns, at 10% over threshold energy with a inlet pressure of 65 psi. As can be seen, a bubble nucleates during the

heater pulse and continues to grow after the voltage applied to the heater is removed as the fluid in the channel continues to remove heat from the heater. After nucleation, the bubble is carried downstream by the flow in the channel both during and after bubble growth. At a certain point, the heat from the heater is insufficient to influence the bubble, and it releases from the heater and is carried downstream to collapse within the exit section of the device.

This bubble behavior has many advantages. First, the bubble is carried downstream of the heater meaning there is no damage to the heater due to bubble collapse. Additionally, it suggests that the heat is more efficiently removed from the heater than in a typical thermal DOD with capillary refill operation. Finally, it explains the high frequencies that can be obtained with the captive CIJ architecture. As seen in Figure 12, the time that the bubble leaves the end of the heater – and not the bubble collapse time – sets the obtainable frequency. Smaller heaters, shorter heater pulses and higher pressures (higher velocity flow) led to higher obtainable drop formation frequencies.

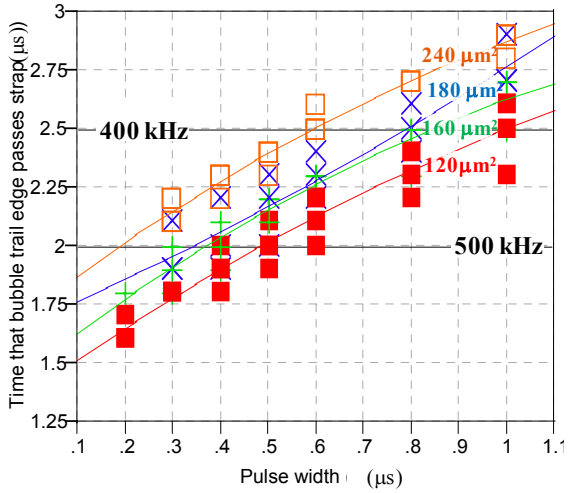

Figure 12. *Predicted maximum drop generation frequency calculated from the time that the bubble clears the heater as a function of pulse width applied to the heater at 65 psi.*

Captive CIJ: Device Design, Fabrication and Evaluation

The next step was to combine these leanings with additional guidance from further CFD modeling into an integrated device. The primary goal in fabricating these third experimental devices was to prove the feasibility of a single device to have robust drop formation and captive flow before and after a drop formation event. Additionally the devices were designed to probe the effect of various geometric parameters on drop performance and captive flow. A design of experiments was used and over 800 unique devices were fabricated. These devices also provided a platform for evaluating the impact of operating parameters on performance. In addition to the experimental variations in geometry, a predicted best design was used to fabricate die with a printable geometry having a 600 npi 32 nozzle array that was used to make an initial evaluation on printing with the captive CIJ architecture.

These devices were fabricated using standard MEMS processes using the preferred chamber design from the captive flow experiment and the angled bore, wider channels and larger heaters from the drop formation experiment. The process used were the same as those discussed above, only the heaters were TaSiN. Figure 13 shows captive drop formation at 10 kHz. The location of the bore is between the yellow dashed lines at the right of the image, and a large vent begins at the green line and continues off the end of the image. The image clearly shows that under the correct operating conditions it is possible to launch a drop without causing the channel to flood. It is worth noting that it is more difficult to keep fluid captive with the dynamics of drop formation, which results in a smaller (but viable) operating space for captive flow.

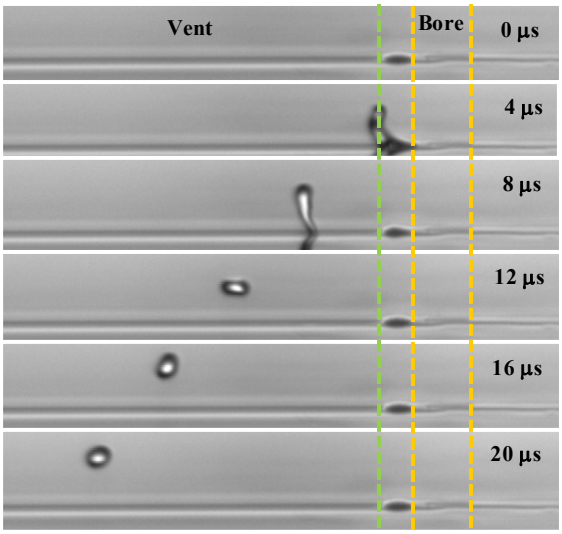

Figure 13. *Captive 10 kHz drop formation at a series of delay times.*

Figure 14 shows captive drop formation at 100 kHz. The top plane of the device channel is identified by the yellow dashed line (drops below the line are reflections). The image was captured at a delay of 12 μs, and the drops were formed at 65 psi and 10% over threshold energy with a 0.5 μs pulse.

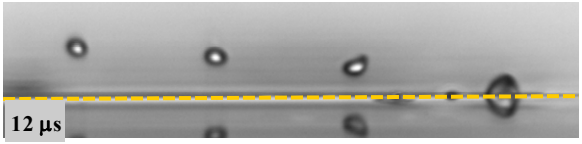

Figure 14. *Captive drop formation at 100 kHz.*

The images shown in Figures 13 and 14 were generated with single channel experimental variations. Within the design of the experiment there were a number of channels that had excellent drop formation and captive behavior. Fortunately, the previous experiments provided sufficient guidance to yield working 32 nozzle array devices. The devices are sub-optimum, but did allow us to experimentally verify that it was possible to put ink to paper with this new drop generator architecture.

Figure 15 is a composite image (post processing) showing the drop trajectory of one nozzle of a printable array. As can be seen

©2013; Society for Imaging Science and Technology

from the image, this design gave stable drop formation but generated unwanted satellites. The primary print drop volume was 3 pL. Using the same conditions as in the drop imaging, a number of prints were made. The paper speed of our experimental setup was limited to 100 fpm. This limited the maximum drop formation frequency to 12 kHz in order to obtain 600 x 600 dpi images.

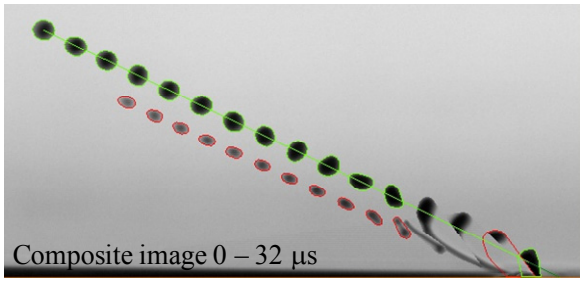

Figure 15. *Drop formation from a single nozzle of a 32 jet array; image is composite of strobe delay times from 0 to 32 μs in 2 μs increments.*

Figure 16 shows two print patterns generated using these conditions. Both images are 600 x 600 dpi, the lack of fill in black areas is due to the undersized drops for this resolution. The image on the left is a 6 pixel by 6 pixel checkerboard pattern, and the right hand image contains one pixel lines separated by 5 pixel lines. The images show a consistent array signature, indicating that while there were nozzle to nozzle differences each nozzle was self consistent. This illustrates that each nozzle can reproducibly generate print drops. Additionally, while the expected drops from the satellites can be seen in the images there are no areas that exhibit print artifacts that would be associated with a failure in the captive flow. Generally, print results were consistent with what was expected from the visualization of drop generation. This strong correlation leads us to believe that quality prints could be generated from optimized captive CIJ devices.

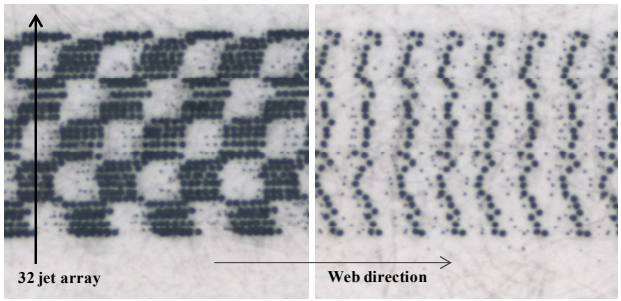

Figure 16. *Images of prints made with a fully integrated captive CIJ device at 12 kHz and 100 fpm. Images were taken using an ImageExpert handheld device.*

Conclusions

The first two experiments independently demonstrated the key aspects of the captive CIJ technology and provided the data necessary for the integrated device design. It was also shown that a range of drop volumes was possible, including drops as small as 0.5pL. Further analysis of the thermal bubble deflection mechanism brought an understanding that the captive CIJ architecture is possible of very high frequency drop generation with experimental demonstration up to 500kHz.

Using complete captive CIJ devices we were able to experimentally show the potential for captive CIJ as a viable print architecture. The drop formation and captive flow behavior was similar to what was found in the earlier component technology devices, and the large number of device variations provided a number of devices with the correct geometric parameters to manage the fluidic interactions between drop formation and the captive flow. As shown, some experimental variations were able to generate satellite free print drops, while otherwise maintain captive flow conditions. We were able to use the printable devices fabricated in this experiment to print patterns (ink-to-paper) with the captive CIJ architecture.

Acknowledgments

The authors thank the staff of Kodak's microfabrication and micropackaging laboratory within the Kodak Technology Center for their contributions on device fabrication and packaging. Additional device fabrication was done at the Cornell NanoScale Science & Technology Facility (CNF) in Ithaca, NY, at Smart System Technology & Commercialization Center (STC) in Canandaigua, NY, and at EVG in Phoenix AZ. The authors are grateful for the device characterization work carried out by Ronald Oyer and the test fixture design and build of Thomas Palone.

References

[1] Y. Xie, J. Jech Jr and M. J. Piatt, U.S. Patent No. 8,201,924. "Liquid Diverter for Flow Through Drop Dispenser" (2012).
[2] Y. Xie and J. Jech Jr, U.S. Patent No. 8,172,364. "Flow Through Dispenser Including Improved Guide Structure" (2012).
[3] Y. Xie and J. Jech Jr, U.S. Patent No. 8,118,408. "Flow Through Dispenser Having Different Cross-Sectional Areas" (2012).
[4] Y. Xie, C. R. Ellinger, M. J. Lehmann, J. Jech Jr, and Q. Yang, U.S. Patent Application No. 20120098907. "Liquid Dispenser Including Curved Vent" (2012).
[5] Y. Xie and J. Jech Jr, U.S. Patent Application No. 20120098888. "Liquid Dispenser Including Curved Outlet Opening Wall" (2012).

Author Biography

Carolyn Ellinger received the B.S. degree in chemical engineering from the State University of NY at Buffalo, where she was a Kodak Fellow; and an M.S. degree in chemical engineering from the University of Rochester. She joined Eastman Kodak Company, Rochester, NY, in 1997, holding technical positions in film and paper systems, flexible displays, nanotechnology semiconductor devices, MEMS-based inkjet printhead design and fabrication, inkjet printhead characterization, and functional printing. She is currently in the Kodak Aligned Technology Center.

Yonglin Xie received a B.S. and a M.S. degree in physics from Peking University. He received a Ph.D. degree in physics from Boston University, and an executive MBA degree from the Simon School of Business at the University of Rochester. Prior to joining Kodak in 2005 (-2013), he held positions at Peking University, Xerox Corporation, and Trident – An ITW Company. He is currently a professor at the Chinese Academy of Sciences.